Grid Fault Performance of Brushless Doubly-Fed Reluctance Machines in Wind Turbine Applications

D. Gay[1], R.E Betz[2], D. Dorrell[3], A. Knight[4]
[1,2]School of Electrical Engineering and Computing, University of Newcastle, Australia,
[3]University of KwaZulu-Natal, Durban, South Africa.
[4]Department of Electrical and Computer Engineering, University of Calgary, Alberta, Canada,
email:[1]David.Gay@newcastle.edu.au; [2]Robert.Betz@newcastle.edu.au;
[3]dorrelld@ukzn.ac.za; [4]Andy.Knight@ucalgary.ca

Keywords

<<Brushless Doubly Fed Reluctance>>, <<DFIG>>,<<Wind Turbine>>,<<Grid Fault>>

Abstract

The DFIG and the BDFRM have very similar dynamic equations, however the BDFRM's complex flux coupling produces machine parameters very different to the DFIG. These parameter differences result in different intrinsic machine behaviour under fault conditions. This paper develops and uses a simple model to explain the fault performance differences between the machines, and then verifies these predictions using a combination of simulation and experimental results. The general conclusion is that the intrinsic large leakage inductances of the BDFRM assist with protecting the rotor side converter during grid side fault conditions.

Nomenclature

$\underline{\lambda}_{p,s}$ Primary and secondary winding stationary frame flux linkage space vectors.
$\underline{\lambda}_{pr,sr}$ Primary and secondary winding rotating frame flux linkage space vectors.
$\underline{x}$ Denotes a stationary frame space vector x.
$\underline{x}_r$ Denotes a synchronously rotating frame space vector x.
$i_{p,s}$ Primary and secondary winding stationary frame current space vectors.
L_p Primary or grid winding self inductance.
L_s Secondary or rotor winding self inductance.
$L_{lp,s}$ Primary and secondary leakage inductances.
L_{ps} Mutual inductance between primary and secondary windings.
s Slip defined as $\frac{\omega_p - \omega_r}{\omega_p}$
BDFRM Brushless Doubly Fed Reluctance Machine
DFIG Doubly Fed Induction Generator
GC – Grid Code.
RSC – Rotor Side Converter.
TSO – Transmission System Operator.
WEC – Wind Energy Converter.
WRIM – Wound Rotor Induction Machine.

1 Introduction

Wind energy converter (WEC) capacity is now in excess of 500GW globally. The year 2016 saw a 12.6% growth in cumulative capacity, with countries opting for a mix of land based and offshore systems [1]. With increased penetration, transmission system operators (TSOs) require increased grid stabilisation capabilities in emerging WEC technologies. Grid codes (GCs) for wind farms are now approaching the requirements for traditional synchronous generation as TSOs respond to the growing popular demand for greater renewable energy penetration.

Technologies employing different generators, including doubly fed induction generators (DFIGs) and permanent magnet generators (PMGs), combined with new power electronic converter topologies have emerged as a result. DFIG based WECs using partially rated converters have dominated the market to date due to lower cost, however PMG based WECs using fully rated converters are gaining market share due to fault tolerance and easier compliance with GCs [2].

An issue for DFIG based WECs is potential rotor side converter (RSC) failure during grid or wind farm fault conditions. Being partially rated, the RSC is typically designed to handle ± 0.3pu of the total wind turbine power [3]. RSC voltages and currents exceeding converter ratings (either voltage, current or both) can occur when the grid voltages rapidly change during system faults. Both symmetrical and asymmetrical faults of varying depth attempt to change the grid produced flux, causing both RSC and DC bus issues in the connected power electronics. Solutions to the RSC problems have historically involved short circuiting or crowbarring the rotor windings as shown in Fig. 1 [2, 3]. The configuration and control of crowbar circuits has been actively studied since the 1990s. Shorting the rotor circuit configures the DFIG as a Wound Rotor Induction Machine (WRIM). Whilst robust, the induction machine connection does not allow reactive power support during the fault, and potentially contributes to voltage dips by consuming reactive power [3].

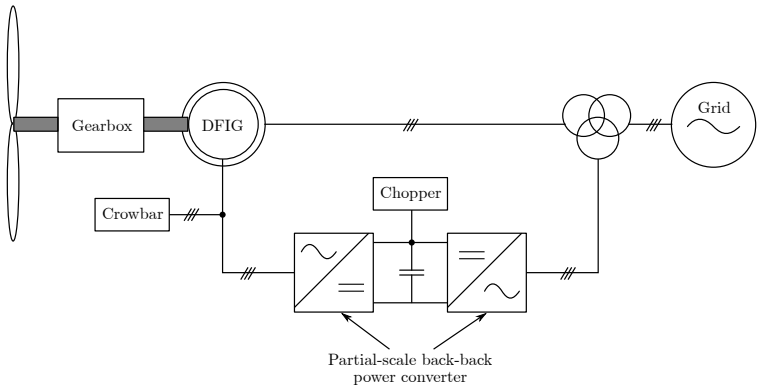

Fig. 1: DFIG based WEC with Crowbar [4]

A potential competitor machine for the DFIG is the Brushless Doubly-Fed Reluctance Machine (BDFRM). This machine has virtually the same dynamic equations as the DFIG, both being doubly fed. Unlike the DFIG, both BDFRM windings are on the stator of the machine - there are no brushes. The rotor, as the name of the machine implies, is a reluctance rotor. One of the stator windings assumes the role of grid connected winding, and the other functions as the rotor converter connected winding. These windings are mutually coupled via a path involving the rotor reluctance. The windings and the reluctance rotor have different pole numbers. Through a complex modulation process, the rotor bidirectionally converts the winding pole numbers so that a variation of mutual inductance with rotor angle occurs between the windings. This results in torque production. This process is briefly outlined in the next section. A key difference between the DFIG and the BDFRM is that the latter does not have any slip rings making the machine extremely robust and reliable. As with the DFIG, it can operate as a doubly fed machine, an induction machine or a synchronous machine depending on how the converter side winding is configured.

Typical parameters for a range of DFIG machines are presented in Table I. These were taken from the wide body of literature concerning RSC fault current mitigation. BDFRM parameters measured in [5] are included in the last column for comparison. As found in [5] the BDFRM has a very large asymmetry in the leakage inductances. This paper carries out a preliminary investigation into the effects of these parameters on rotor side currents under grid side fault conditions. The motivation for this investigation is the prospect that the intrinsic inductance values of the BDFRM will assist in minimising the deleterious effects of grid side faults on the

Table I: Typical DFIG and BDFRM Parameters

TYPE	DFIG	DFIG	DFIG	DFIG	DFIG	BDFRM
Size (kW)	15	1500	1500	2000	2300	16
Voltage (V)	380	575	575	690	690	400
L_M (pu)	1.367	2.9	2.175	3.9528	6.921	2.733
L_{LS} (pu)	0.088	0.171	0.1282	0.0924	0.257	0.2828
L_{LR} (pu)	0.088	0.156	0.117	0.0996	0.295	5.1838
R_S (pu)	0.0151	0.0071	0.0064	0.0049	0.0175	0.0634
R_R (pu)	0.0167	0.0058	0.0022	0.0055	0.019	0.0734
Pole Pairs	2	3	2	2		n/a

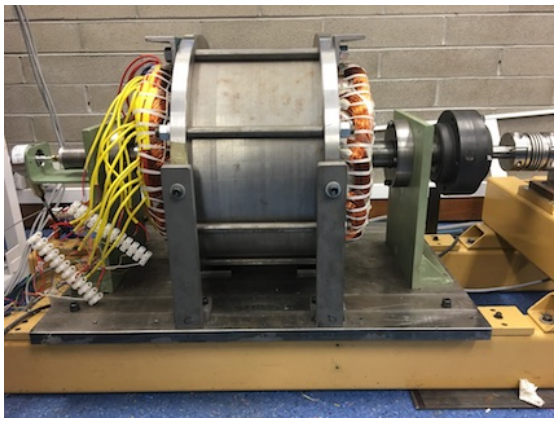

(a) Experimental BDFRM

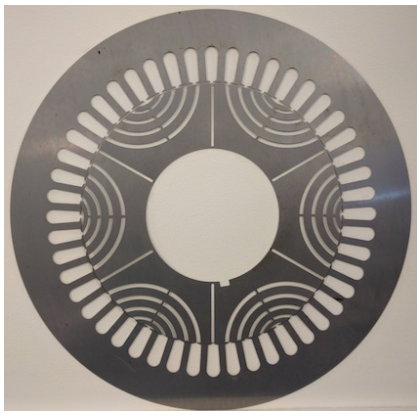

(b) BDFRM stator and rotor laminations

Fig. 2: BDFRM stator and rotor laminations showing flux barriers

RSC.

2 BDFRM and DFIG dynamic equations

The experimental BDFRM (Figure 2a) that forms the basis of this investigation is a 16kW machine with a 48 slot stator in which an 8 pole primary (grid) and 4 pole secondary (RSC) winding are wound. A 6 pole reluctance rotor with radial laminations and flux barriers couples flux between the windings, as reported in [6]. Figure 2b shows the stator and rotor laminations for this machine.

Detailed mathematical modeling for the BDFRM appears in [7,8] and for space reasons will not be repeated in this paper. It can be shown [8] that there is a rotor pole number p_r such that one of the harmonic fluxes from each winding rotates at the same angular velocity and has the same pole number as the fundamental flux density waveform for the other winding. It is through this mechanism that coupling is created between the different pole number windings. In [8] it is shown that $p_r = p + q$, where p and q are the pole pairs of the primary and secondary windings respectively. Under this condition the rotation angular velocity of the machine is $\omega_{rm} = \frac{\omega_p + \omega_s}{p_r}$, where ω_p is the primary winding (or grid) frequency, ω_s is the secondary (or RSC) frequency, and ω_{rm} is the mechanical shaft angular velocity. The effect of the reluctance rotor modulation is a spatial and temporal heterodyning of winding mmfs (similar to heterodyning in communications), which allows the windings to magnetically couple and generate torque.

Another relevant point about the machine structure is that the reluctance path of the higher pole number winding is effectively double that of the lower pole number (for the 8, 4 pole winding machine under investigation), all of which contribute to the asymmetrical leakage inductances reported in [9] and established experimentally in [5].

The derivation of the BDFRM space vector dynamic equations can be found in [7,8,10] and

are presented here in (1) to (4) for a reference frame rotating at the grid angular frequency ω_p .

$$\underline{v}_{pr} = R_p \underline{i}_{pr} + \frac{d\underline{\lambda}_{pr}}{dt} + j\omega_p \underline{\lambda}_{pr} \tag{1}$$

$$\underline{v}_{sr} = R_s \underline{i}_{sr} + \frac{d\underline{\lambda}_{sr}}{dt} + j(\omega_r - \omega_p)\underline{\lambda}_{sr} \tag{2}$$

$$\underline{\lambda}_{pr} = L_p \underline{i}_{pr} + L_{ps} \underline{i}^*_{sr} \tag{3}$$

$$\underline{\lambda}_{sr} = L_s \underline{i}_{sr} + L_{ps} \underline{i}^*_{pr} \tag{4}$$

where $L_{p,\,s,\,ps}$ are the self and mutual three-phase inductances of the primary and secondary windings. The complex conjugate currents in (3) and (4) result from the heterodyning action of the BDFRM rotor. Note that (1) and (2) are in different reference frames (ω_p and $\omega_r - \omega_p$ where $\omega_r = p_r \omega_{rm}$) . If $\omega_p = 0$, the primary winding now has a stationary reference frame while the secondary winding becomes the effective rotor reference frame, as per the stationary frame DFIG model.

Even though the underlying magnetic principles are completely different, the DFIG and BDFRM dynamic models are very similar. This means that simulation studies of both the DFIG and BDFRM grid fault effects can be completed using the same model, with only parameter changes and minor system changes to reflect the machine type.

3 Parameter effects on winding fault currents

Even though the DFIG and BDFRM models are dynamically the same, the parameters in the BDFRM are vastly different to the DFIG. DFIGs have parameters that are typical of most induction machines (as it is essentially a wound rotor induction machine). The rotor and stator leakages in the DFIG are usually very similar in value and around 0.1 to 0.2 pu (See Table I). The significant difference between the DFIG and BDFRM parameters is the relatively large leakage inductances in the later, especially on the secondary (or converter) side of the machine [5]. The experimental machine, for example, has a per unit leakage inductance on the secondary winding of $L_{ls} = 5.2$ pu.

Based on [11], the following analysis demonstrates the effect these parameter differences have during grid fault conditions. Writing the raw equations for the DFIG/BDFRM in stationary frame space vectors

$$\underline{v}_p = R_p \underline{i}_p + \frac{d\underline{\lambda}_p}{dt} \tag{5}$$

$$\underline{v}_s = R_s \underline{i}_s + \frac{d\underline{\lambda}_s}{dt} \tag{6}$$

where the fluxes can be written as (in DFIG form)

$$\underline{\lambda}_p = L_p \underline{i}_p + L_{ps} \underline{i}_s \tag{7}$$

$$\underline{\lambda}_s = L_s \underline{i}_p + L_{ps} \underline{i}_p \tag{8}$$

From the flux equations it is a simple manipulation to get the following expression:

$$\underline{\lambda}_s = \sigma L_s \underline{i}_s + \frac{L_{ps}}{L_p} \underline{\lambda}_p \tag{9}$$

where $\sigma = \frac{L_p L_s - L_{ps}^2}{L_p L_s}$ is the leakage coefficient.

Substituting (9) into (6) and expanding provides

$$\begin{aligned} \underline{v}_s &= R_s \underline{i}_s + \frac{d\underline{\lambda}_s}{dt} \\ &= R_s \underline{i}_s + \left(\frac{L_s L_p - L_{ps}^2}{L_p} \right) \frac{d\underline{i}_s}{dt} + \frac{L_{ps}}{L_p} \frac{d\underline{\lambda}_p}{dt} \end{aligned} \tag{10}$$

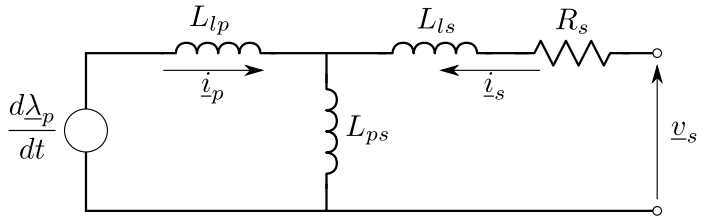

Fig. 3: Equivalent circuit for the BDFRM and DFIG rotor.

Using (7) we can write

$$\frac{L_{ps}}{L_p}\underline{\lambda}_p = L_{ps}\underline{i}_p + \frac{L_{ps}^2}{L_p}\underline{i}_s$$

which can be substituted into (10) and, after some manipulation we obtain

$$\begin{aligned} \underline{v}_s &= R_s\underline{i}_s + L_s\frac{d\underline{i}_s}{dt} + L_{ps}\frac{d\underline{i}_p}{dt} \\ \therefore \underline{v}_s &= R_s\underline{i}_s + L_{ls}\frac{d\underline{i}_s}{dt} + L_{ps}\left(\frac{d\underline{i}_s}{dt} + \frac{d\underline{i}_p}{dt}\right) \end{aligned} \tag{11}$$

The other half of the circuit can be written from (7) by differentiating it to give

$$\frac{d\underline{\lambda}_p}{dt} = L_{lp}\frac{d\underline{i}_p}{dt} + L_{ps}\left(\frac{d\underline{i}_p}{dt} + \frac{d\underline{i}_s}{dt}\right) \tag{12}$$

Equations (11) and (12) allow the equivalent circuit for the rotor side of the DFIG and BDFRM to be constructed as shown in Figure 3.

The interpretation of Figure 3 follows that presented in [11]. Under normal grid conditions $\underline{\lambda}_p$ is rotating at the supply frequency. Assuming that the rotor is rotating at ω_r electrical radians/sec, then $\underline{\lambda}_p$ is rotating at $s\omega_p$ r/s relative to the rotor. Converting $\underline{\lambda}_p$ to the rotor frame, we can write $\underline{\lambda}_{pr} = \lambda_p e^{j(\theta_p - \theta_r)}$. Consequently,

$$\frac{d\underline{\lambda}_{pr}}{dt} = e^{j(\omega_p-\omega_r)t}\left(\frac{d\lambda_p}{dt}\right) + j(\omega_p - \omega_r)\underline{\lambda}_{pr} \tag{13}$$

where the first term reflects the flux amplitude change, and the second term the rotation of the primary flux relative to the rotor. If there is a short circuit grid fault then the primary flux will stop rotating, i.e. $\omega_p = 0$, and the second term in (13) will become $-j\omega_r\underline{\lambda}_{pr}$. Since $\omega_r \gg \omega_{sf}$, where $\omega_{sf} = \omega_p - \omega_r$ *the voltage produced by the faulted primary flux will be much larger than the normal non-fault level.* In addition to this rotational voltage there will be a voltage due to the rate of collapse of the flux in the primary winding (the first term of (13)).

Considering Figure 3, the L_{ls} inductance and the R_s resistance are an impedance seen by the $\frac{d\underline{\lambda}_p}{dt}$ voltage. Since L_{ls} is very large in the BDFRM compared to the DFIG, for a given induced $\frac{d\underline{\lambda}_p}{dt}$ voltage the $|\underline{i}_s|$ current will be much smaller (assuming $\underline{v}_s$ acts as a voltage source). This conjecture forms the basis for this paper, which postulates the very large secondary leakage inductance in the BDFRM will help prevent the build up of excessive currents in the secondary winding under primary winding grid fault conditions. This in turn will offer more protection for the secondary or rotor side converter when used in double fed applications such as a wind turbine generator. The voltages induced would be clamped by the diode in the RSC to the DC link voltage. Therefore, providing that the energy from the fault condition is not too high, the DC link capacitor should not go over voltage during the fault.

4 Experimental and Simulation Configuration

System experimental constraints were first considered, including system supply with respect to fault currents and reverse power flow. With the fault contactor (3 phase bolted short) applied directly at the BDFRM terminals (a worst case fault condition), line inductors between a

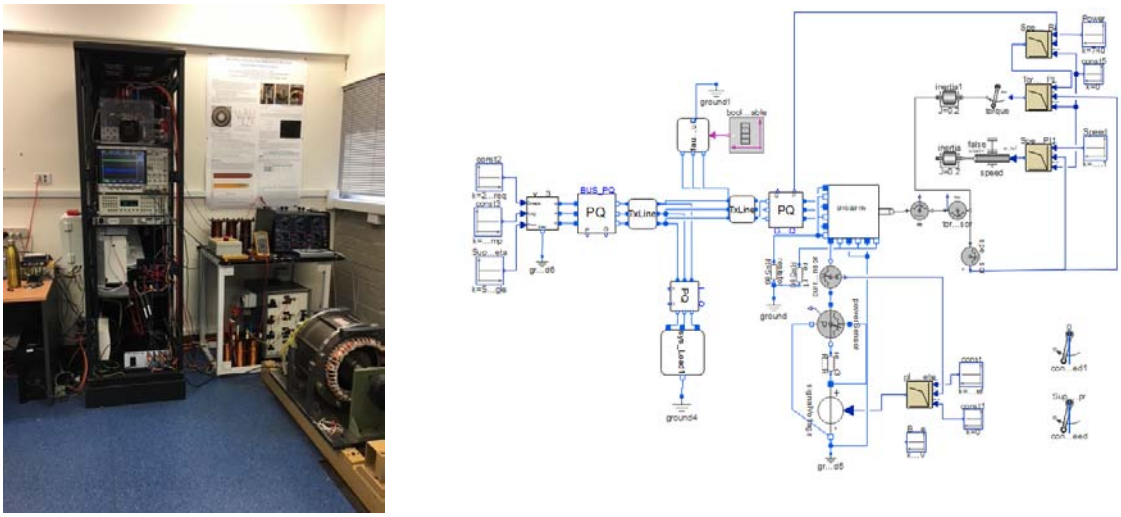

(a) Experimental hardware (b) Simulation diagram

Fig. 4: Experimental hardware

415 / 110V 3 phase transformer and the fault were used to limit grid supply currents to less than 30A. It was experimentally determined that BDFRM generation of greater than 1kW tended to trip the lab supply. A Modelica® simulation was then built using experimental system parameters and parallel simulations and experiments conducted to validate the accuracy of the simulated data. These validation tests included

1. Supply stability and short circuit test - connected line inductors were shorted to assess supply capability.
2. BDFRM connected with open circuit secondary and locked rotor.
3. BDFRM connected with short circuit secondary and locked rotor.
4. BDFRM connected with short circuit secondary and rotor at synchronous speed.

Test data was collected using a Voltech PM3000A power analyser connected to the system supply (BUS_PQ component in Figure 4b). This testing provided confidence that the simulation model reasonably accurately represents the experimental system. Simulation values used for the system line impedance are 53mH and 5.4Ω, which are the measured values of the air cored line inductors used experimentally. Inductance and resistance values of the transmission line between the fault and generator were very small at 1×10^{-7} H and Ω respectively. The experimental system is shown in Figure 4a.

Unlike the system illustrated in Figure 4b, the experimental system is operated as an open loop synchronous generator – i.e. feedback loops to the motive torque source driving the generator shaft have not been implemented. Future experimental work will include this, as research is extended to the BDFRM operating asynchronously to the grid supply as a wind turbine generator. Closed loop simulation was required to match the simulated output with the experimental generator output for accurate comparison.

This study primarily compares RSC currents under fault conditions that differ due to parameter variance between BDFRM and DFIG machines. To ensure clarity in comparison, no initial control will applied to the secondary currents. Experimentally, a 13.3VDC LiFePO4 battery is used as the RSC winding voltage, with the B and C phase windings shorted as the return path. For simulation purposes, this is modeled as an ideal voltage source with an external resistance. This however effectively clamps the RSC voltage.

A second experiment using a VSC with feedback current control is performed. A digital PI field current controller attempts to keep the current at the set-point level. The simulation

controller is implemented with a 200μsec delay to ensure the normal control delays in a digital control system apply. This delay also ensures that the PI control gains cannot be increased to unrealistic values (the system will become unstable if they are). The gains for the PI controller were set up individually for each machine so that the highest control bandwidth without instability was achieved. The output of the PI controller is limited to 600 V, implying a 600 VDC link voltage for the RSC. All experimental current, voltage and control data presented is sampled at 10kHz through the BDFRM Denkinetic® controller.

In simulation, the 15kW DFIG parameters were taken from test results presented in Chapter 5 of [12] and are provided in Table I. Both the 16kW BDFRM and 15kW DFIG simulations are conducted at rated speeds ($\omega_{sf} = 0$, synchronous generator equations apply), with the field current and load angles adjusted to supply approximately 720W of real power and 560VAR of reactive power to the grid prior to fault application.

5 Simulation and Experimental Results

In order to test the intrinsic properties of the machines under fault conditions, the BDFRM simulation pre fault conditions were adjusted to reflect the experimental set up. Equivalent simulations were then carried out for the DFIG, with both machines operating in synchronous mode. This mode of operation makes it easy to see the effects of the grid fault on the RSC windings of both machines. Two sets of results are for the cases where there is (i) no current control on the RSC winding, and (ii) where the RSC current is controlled by a PI controller as described in Section 4.

Remark 1 *The use of the synchronous operation mode allows correct operation of the machines with an uncontrolled RSC. This in-turn allows the behaviour of the currents in the RSC winding to show the effects of the intrinsic coupling between the grid and RSC windings of the two machines. Synchronous mode also allows the use of a simple current controller whose bandwidth can be made more or less the same for the BDFRM and DFIG. Therefore, comparisons of two machines under current control can be directly compared.* ■

Synchronous mode was established by applying direct current to the RSC connected windings of both machines. In the case of the BDFRM the rotor coupled secondary flux will try to align with the grid provided stator flux to make the machine operate in synchronous mode at a specific power angle. As the experimental system was operated open loop, slight differences in rotor and stator flux speed caused a ramp effect in power output until pole slipping occurred. Measurements were therefore taken with a slowly increasing power angle, and the fault applied at a similar power level for each experiment. Figure 5 provides the comparison between experimental and simulation results at the point of fault application. The measured experimental power value just prior to fault application was used as the reference for simulations and the simulated fault application was adjusted in time to ensure the fault occurred at the same point as the experimental voltage waveform. This provides verification of pre fault conditions and allows the experimental and simulated system dynamics to be evaluated resulting from fault application.

Figure 6 shows the measured and simulated secondary A-phase currents for the BDFRM under fault conditions along side the simulated DFIG current. The fault was applied for 1 second to allow a transient response to be recorded, then removed. Figure 6a shows the uncontrolled secondary currents where a battery was used as a voltage source, while Figure 6b shows the RSC controlled currents. Insets of BDFRM measurements in all figures are provided to improve the clarity of the result graphs.

The peak uncontrolled current resulting from the fault application is 8.46pu for the DFIG, and 1.56pu for the BDFRM in simulation, and 2.4pu for the BDFRM experimentally. The peak occurred at the start of the fault with subsequent peaks decaying to pre fault values after 200 milliseconds for all three currents. Peak current excursions for the RSC simulations were 1.54pu for the DFIG and 1.04pu BDFRM, with the experimental BDFRM excursion of 1.05pu.

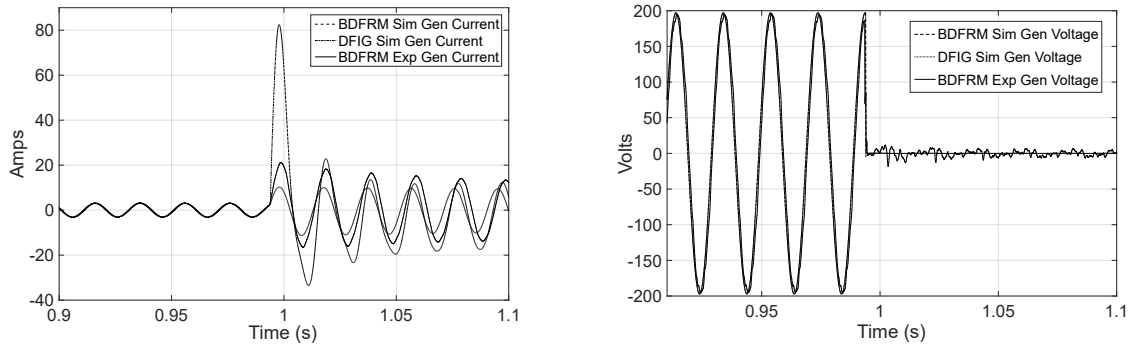

(a) Current measurements. (b) Voltage measurements.

Fig. 5: Comparison of pre and post fault DFIG and BDFRM simulation and experimental grid results.

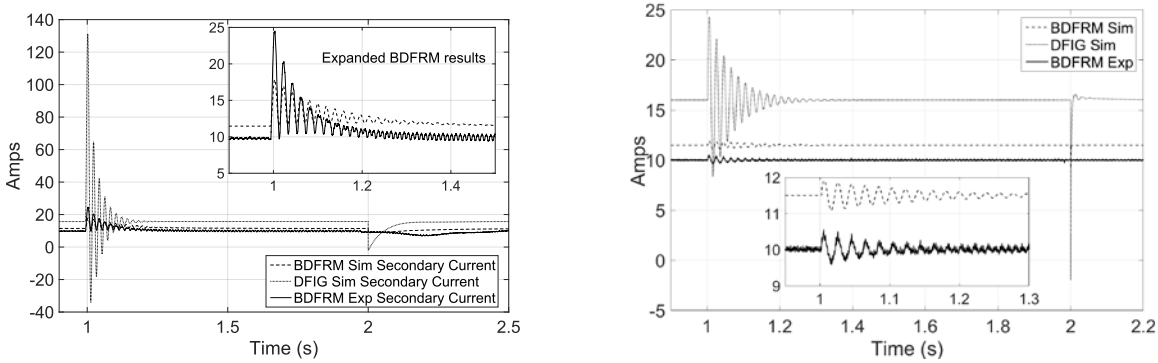

(a) Uncontrolled currents (b) Controlled Currents

Fig. 6: Secondary A-phase currents during grid fault.

Remark 2 *One can see from the results in Figure 6 that the currents in the BDFRM are substantially smaller in PU terms than those in the DFIG. In fact, the BDFRM currents under the fault are not substantially different than those before the fault. Taking into consideration the modeling limitations, the simulated and experimental BDFRM results agree reasonably well.* ■

Under both battery and RSC secondary supply, it should be noted the BDFRM experimental currents appear to contain higher order harmonic content (probably due to winding harmonics), as well as inverter switching noise for the RSC controlled currents. Figure 7 shows the RSC secondary applied voltage during the fault.

Insets in Figure 7 emphasise the differences between results at the point of fault application and release. On removal of the fault (at 2.0003 seconds), the BDFRM simulation A-phase voltage reached the RSC DC bus limit of 600V for 2 milliseconds, while the DFIG reached 554V for under a millisecond but decayed at a slower rate. Experimentally, the fault was lifted at 1.983 seconds and the secondary A-phase voltage rose to 77V (590V DC bus on RSC inverter).

6 Discussion

As shown by Figure 5, the simulation modeled the experimental system pre-fault very accurately. Differences in BDFRM simulation and experimental results post fault are a function of two principle areas.

1. Differing control mechanisms for the machine rotor speed, and
2. flux coupling effects between secondary and primary windings in the experimental BDFRM that are not captured in the simulation machine equations.

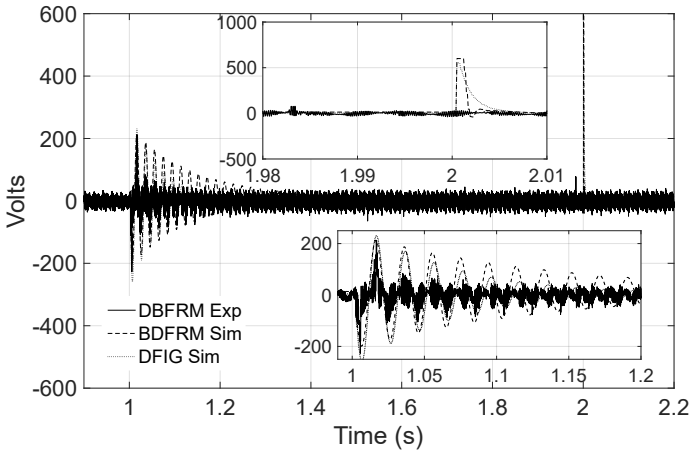

Fig. 7: Secondary A phase voltage

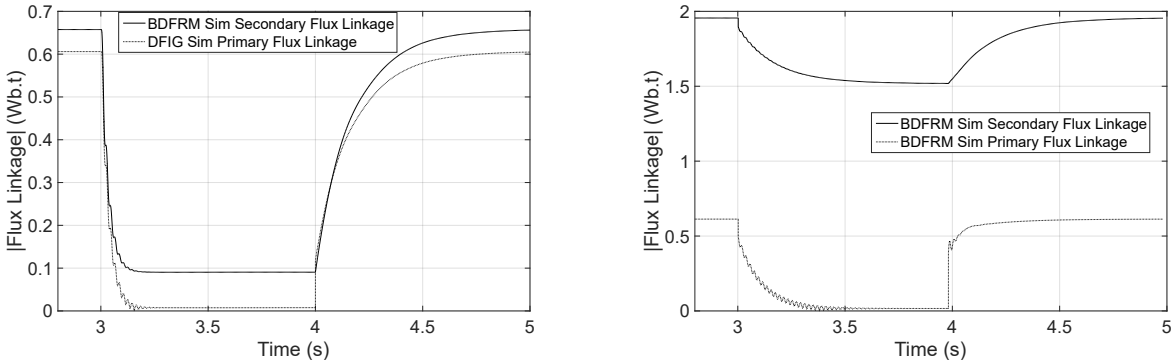

(a) DFIG Flux Linkage (b) BDFRM Flux Linkage

Fig. 8: BDFRM and DFIG flux linkages

The influence of point 1 can be seen in Figure 5a as the experimental current frequency decreases due to load torque increase from fault application. The control algorithm response of the DC drive, set to closed loop speed control, was far slower than the simulation response. While this does not impact on the validity of these results, using the drive in closed loop torque control mode is being considered for future work. Converting the simulation to speed control an identical ramp effect could be achieved, however it increased the simulation times dramatically.

Some aspects of point 2 are presented in [5]. The details of these effects are the subject of ongoing research. It appears that space harmonics due to physical winding constraints, also modulated by the rotor, additionally couple to opposite winding space harmonics adding to the fault current magnitude. Evidence of this can be seen in Figure 7, where the control voltage applied to the secondary winding has sinusoidal components in its effort to produce direct current.

Results shown in Figure 6a indicate the natural current limiting effect of the BDFRM parameters. Simulation primary and secondary flux linkage magnitudes $|\underline{\lambda}_p|$ and $|\underline{\lambda}_s|$ at the time of fault application for the BDFRM and DFIG are shown in Figure 8. The difference in secondary flux linkage values between machines is due to the size of inductance parameter values (49.5mH and 188mH) and applied secondary currents (16A and 11.5A) for the DFIG and BDFRM respectively.

Remark 3 *An immediate observation to be made from Figures 8a and 8b is the flux linkage decay rate in the DFIG is much greater than the BDFRM. This would tend to make the induced* $\frac{d\lambda}{dt}$ *voltage higher in the DFIG as compared to the BDFRM.*

With the slower decay in the BDFRM and given the small change in rotor speed during the

fault, the voltage across the secondary winding ($j\omega_R|\lambda_p|$ in (13)) for the BDFRM will however remain higher for longer, as evidenced by the greater control effort applied to the secondary winding of the BDFRM, shown in Figure 7.

7 Conclusions

This paper explored the potential protection offered by the BDFRM to the RSC of a wind turbine generator system when there is a three phase grid fault. The performance of the BDFRM was compared to that of a similar size DFIG under the same fault conditions.

It was found that the large leakage inductances that are intrinsic to the BDFRM design do significantly reduce the currents flowing into the RSC under a three phase fault condition, compared to the DFIG. A combination of theory, simulation and experimental results were used to arrive at this conclusion.

References

[1] G. W. E. Council, "Global wind report-annual market update," tech. rep., Global Wind Energy Council, 2016.

[2] M. B. C. Salles, K. Hameyer, J. R. Cardoso, A. P. Grilo, and C. Rahmann, "Crowbar system in doubly fed induction wind generators," *Energies*, vol. 3, pp. 738–753, 2010.

[3] J. Yang, J. E. Fletcher, and J. O'Reilly, "A series-dynamic-resistor-based converter protection scheme for doubly-fed induction generator during various fault conditions," *IEEE Transactions on Energy Conversion*, vol. 25, pp. 422–432, June 2010.

[4] Y. M. Alsmadi, L. Xu, F. Blaabjerg, A. P. Ortega, and A. Wang, "Comprehensive analysis of the dynamic behavior of grid-connected dfig-based wind turbines under lvrt conditions," in *Energy Conversion Congress and Exposition (ECCE), IEEE*, Energy Conversion Congress and Exposition (ECCE), 2015 IEEE, 2015.

[5] D. Gay, R. Betz, D. Dorrell, and A. Knight, "Brushless doubly fed reluctance machine parameter determination," in *IEEE International Conference on Electric Machines and Systems*, Sept 2017.

[6] A. Knight, R. Betz, and D. Dorrell, "Design and analysis of brushless doubly fed reluctance machines," *Industry Applications, IEEE Transactions on*, vol. 49, pp. 50 –58, jan.-feb. 2013.

[7] R. Betz and M. Jovanović, "Introduction to brushless doubly fed reluctance machines - the basic equations," Tech. Rep. EE0023, Department of Electrical Engineering, University of Newcastle, Australia, April 1998. Available on ResearchGate.

[8] R. Betz and M. Jovanovic, "Introduction to the space vector modelling of the brushless doubly fed reluctance machine," *Electric Power Components and Systems*, vol. 31, August 2003.

[9] A. Knight, R. Betz, W. Song, and D. Dorrell, "Brushless doubly-fed reluctance machine rotor design," in *Energy Conversion Congress and Exposition (ECCE), 2012 IEEE*, pp. 2308 –2315, sept. 2012.

[10] F. Liang, L. Xu, and T. Lipo, "D-q analysis of a variable speed doubly AC excited reluctance motor," *Electric Machines and Power Systems*, vol. 19, pp. 125–138, March 1991.

[11] D. Xiang, L. Ran, P. Tavner, and S. Yang, "Control of a doubly fed induction generator in a wind turbine during grid fault ride-through," *IEEE Transactions on Energy Conversion*, vol. 21, pp. 652 –662, Sept. 2006.

[12] G. Abad, J. Lopez, M. A. Rodriguez, L. Marroyo, and G. Iwanski, *Doubly Fed Induction Machine: Modeling and Control for Wind Energy Generation*. John Wiley & Sons, Inc, 2011.